

Testbed design and high-contrast demonstration with the AstroPIC integrated photonic coronagraph

Rachel Morgan^{a,b}, Eduardo Bendek^{a,b}, Ruslan Belikov^b, Kevin Fogarty^b, Anne R. Kroo^c, Carson Valdez^c, Marek Vlk^c, David A. B. Miller^c, Olav Solgaard^c, and Dan Sirbu^b

^aSETI Institute, Mountain View, CA 94043, USA

^bNASA Ames Research Center, Moffett Field, CA 94035, USA

^cStanford University, Stanford, CA 94305, USA

ABSTRACT

Integrated photonics is a promising coronagraph technology option for exoplanet-imaging missions such as NASA's Habitable Worlds Observatory flagship. It is theoretically capable of achieving better performance than traditional bulk-optic coronagraphs because arrays of integrated interferometers can be controlled to implement any optical function that can be described as a linear operator with a device that is orders of magnitude smaller than the bulk optics equivalent. However, photonic coronagraphs require significant maturation to be ready for a space telescope mission. The AstroPIC project is advancing this technology by developing a proof-of-concept integrated photonic coronagraph based on silicon photonic integrated circuit (PIC) technology.

In this paper, we present the design and implementation of the PIC coronagraph testbed at Ames, which is designed to be capable of measuring the target 100 dB extinction ratio required to observe an Earth-like planet around a Sun-like star. A key feature of the testbed design is the ability to re-image a realistic telescope pupil and couple the light into the PIC with a 2D array of grating couplers. We also present preliminary experimental results with the testbed demonstrating on-chip extinction of a single input channel of 92 ± 0.4 dB (6×10^{-10} contrast) by controlling the first diagonal of a 9-channel full triangular mesh for monochromatic light at 1550 μm wavelength.

Keywords: Coronagraphs, Photonics, Exoplanets

1. INTRODUCTION

Integrated photonics has the potential to revolutionize optical instrumentation for astrophysics missions by fabricating many optical components on a common wafer substrate to produce instruments that are smaller, more robust, and more reconfigurable than bulk optics alternatives.¹ For example, a photonic integrated circuit (PIC) can be designed with an array of cascaded Mach-Zehnder Interferometers (MZIs) in a “mesh” configuration to implement any optical operator,^{2,3} meaning that it can be controlled to become a near-optimal coronagraph at small inner working angles.⁴⁻⁷ By leveraging recent advances in integrated photonics technology, a PIC coronagraph instrument can be orders of magnitude smaller and significantly less mechanically complex than the bulk optics coronagraph instruments designed to date, which has huge benefits for next-generation NASA astrophysics missions such as the Habitable Worlds Observatory.⁸

The AstroPIC coronagraph concept, shown in Figure 1, demonstrates the utility of integrated photonics for exoplanet characterization. End-to-end simulations of the AstroPIC concept predict excellent high-contrast performance at small inner working angles⁹ while being much less sensitive to the telescope pupil shape compared to bulk-optics coronagraph designs.^{10,11} The instrument couples light from a telescope pupil plane into a PIC through a microlens array that samples and focuses the light onto a 2D array of grating couplers. The first AstroPIC instrument chip contains a 9-channel full triangular mesh that can be controlled to sort the input light by spatial mode in order to separate planet light from star light.

Further author information: (Send correspondence to Rachel Morgan and Eduardo Bendek)

Rachel Morgan: rachel.e.morgan@nasa.gov

Eduardo Bendek: eduardo.bendek@nasa.gov

Government sponsorship acknowledged. ©2025. All rights reserved.

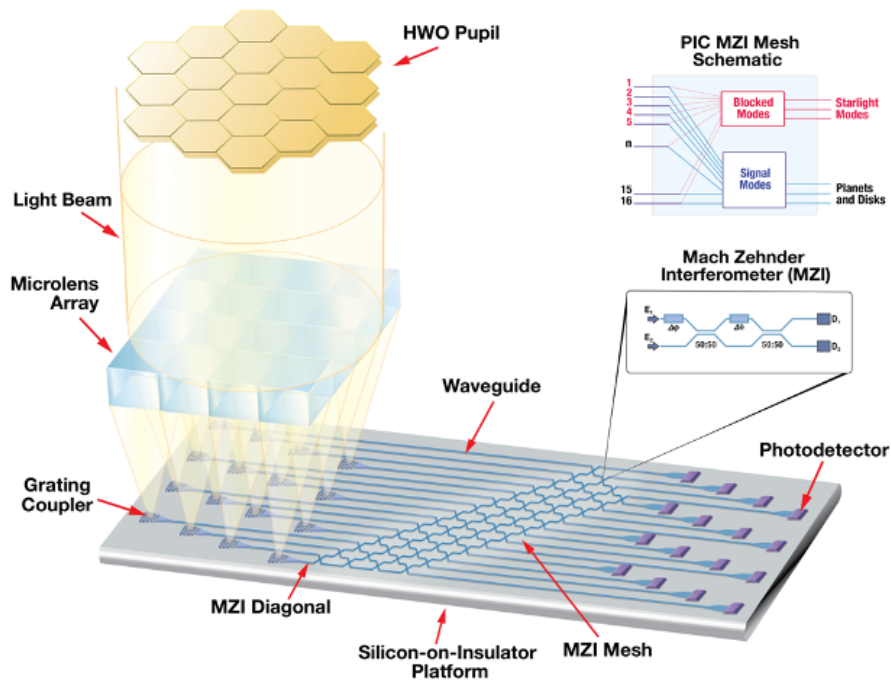


Figure 1. Diagram of AstroPIC coronagraph concept: light is coupled from a telescope pupil plane into an integrated photonic chip using a microlens array and a 2D array of grating couplers. The PIC uses a mesh of MZIs to implement a near-optimal coronagraph operator to separate the planet light from the starlight.

In order to validate this instrument concept, a photonic coronagraph testbed is being developed at NASA Ames Research Center. This paper describes the design, modeling, and implementation of the photonics testbed, as well as preliminary experimental results that demonstrate using the AstroPIC instrument to achieve 87-92 dB extinction of a single illuminated input channel using chip samples fabricated by two different foundries.

2. LABORATORY TESTBED DEVELOPMENT

The primary goals of the AstroPIC testbed are to characterize the performance of the instrument with a realistic telescope pupil aperture and to identify the limiting factors that can be improved in future iterations of the instrument. Specifically, the testbed requirements are to demonstrate contrast sensitivity better than 90 dB (1×10^{-9}) for a single input channel and better than 70 dB (1×10^{-7}) for a realistic HWO-like telescope pupil input. The testbed also needs to be able to measure relevant photonic component test structures to provide data to inform future iterations of the PIC design.

To achieve these goals, the AstroPIC testbed was designed to be able to couple light from free space or optical fibers on and off the chip, control 72 phase shifters and measure the readout from 9 photodetectors simultaneously with >100 dB of dynamic range. The testbed also provides thermal control of the PIC and contains a top-view IR microscope and a side-view visible microscope for alignment and diagnostic visualization.

The key specifications of the testbed design are summarized in Table 1, and a diagram/photo of the testbed is shown in Figure 2.

2.1 PIC Testbed Design

The light source for the testbed is an Optilab TWL-C-B tunable IR laser with a 1530-1565 nm wavelength range and 16 dBm max output power. Light is coupled with a single-mode optical fiber to a Thorlabs U-Bench equipped with a half wave plate and a quarter wave plate for polarization control. Then, a 99:1 fiber coupler is used to tap

Table 1. Key specifications of the AstroPIC coronagraph testbed.

Parameter	Specification
Number of input/output channels	9
Photodetector dynamic range	>100 dB
Number of phase shifters	72
Phase shifter control voltage range	0-10 V
DAQ resolution	16 bits
TEC controller stability	0.01°C
IR microscope pixel size	5 μm
IR microscope resolution	656 \times 520
IR microscope magnification	5 \times

1% of the light to be measured with a monitor photodiode (Thorlabs DET01CFC). The other 99% of the light is coupled to either the free-space coupling optics (described below) or a cleaved single-mode fiber mounted on a custom fiber mount that holds the fiber at an input angle of 12° from the chip surface normal to couple into the grating couplers. Both input configurations are designed to be mounted to a Thorlabs NanoMax™ 3-axis stage with differential micrometer control for alignment. Light is coupled off the PIC with a single cleaved fiber or a fiber array that is aligned with a Thorlabs NanoMax™ 6-axis stage to a line of grating couplers at the output of the mesh. In the future, chips will be packaged with the fiber array bonded to the PIC so that the 6-axis stage can be used to align the microlens array to optimize coupling into the input grating couplers.

The PIC is epoxied and wirebonded to a PCB that transmits the phase shifter control signals from an input connector onto the chip. The phase shifters are controlled with a NI PXIe-6361 data-acquisition unit (DAQ) with two PXIe-6739 cards installed to provide 128 control channels. Each channel has a voltage output of ± 10 V with 16 bit resolution. The PCB is mounted to a custom aluminum plate that contains a cutout underneath the PIC for a Peltier cooler that is controlled with an Arroyo 5240 TEC controller that can maintain a temperature set point to within 0.01° C for a thermistor located on the PCB. The PCB includes thermally conductive vias underneath the PIC and thermal paste is applied between the PCB and the TEC to enhance thermal coupling.

Each of the 9 output channels of the mesh can be coupled to an individual photodetector. Most channels are designed for relatively high incident powers, corresponding to the stellar spatial modes that are orders of magnitude brighter than the signal planet modes. These channels are coupled to 8 Thorlabs DET01CFC InGaAs detectors with variable resistance terminators that are measured to have a sensitivity range of ~ 7 nW - 5 mW. One output channel is designated as the “high-contrast” channel and is coupled to a high sensitivity photodetector (Femto OE-200-IN2-FC) with a variable gain amplifier that provides a measurement range of ~ 100 fW - 2 mW.

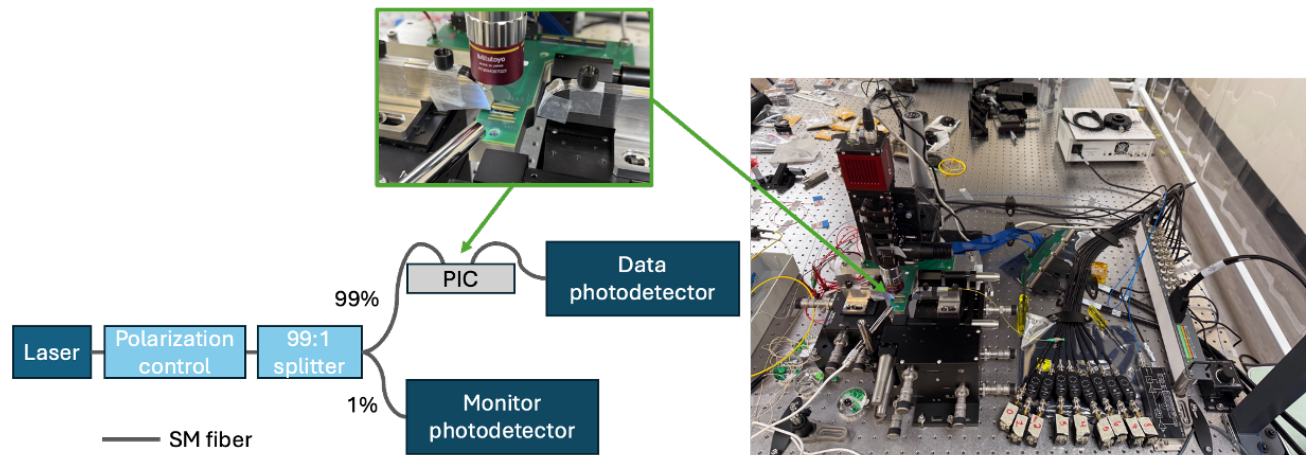


Figure 2. (Left) Diagram of AstroPIC experimental setup. (Right) Photo of the AstroPIC photonics testbed setup at NASA Ames with inset showing a zoom-in on the PIC/PCB with an input fiber mount aligned to the chip.

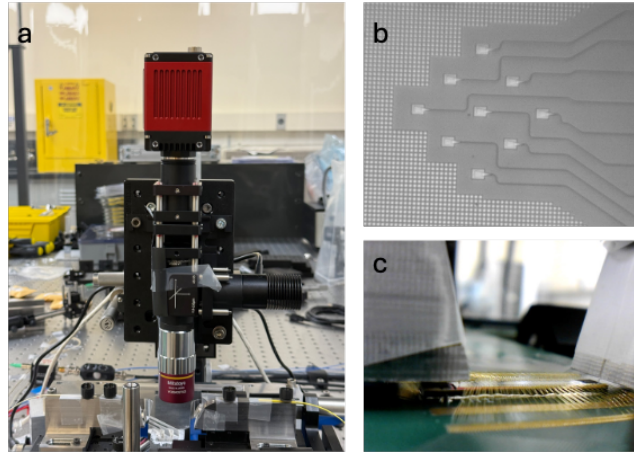


Figure 3. (a) Photo of NIR microscope that provides top-view visualization of the PIC. (b) Photo taken with NIR microscope of the input 9-channel grating coupler array on the PIC. (c) Photo taken with the side-view visible light borescope of optical fibers aligned to couple light to/from the PIC.

The photodetector signals are measured with a NI-2090A BNC breakout attached to a NI PXIe-6361 card installed in the PXIe DAQ. The PXIe-6361 card measures voltages up to ± 10 V with a minimum sensitivity range of ± 0.1 V with 16 bit resolution. With the maximum gain of 10^{11} V/W applied to the Femto photoreceiver, this translates to a resolution-limited detection limit of $\sim 3 \times 10^{-17}$ W, which is much lower than the detector DC noise limit of ~ 100 fW. In the current experimental configuration using single optical fibers for input/output from the chip, we only measure one output channel at a time using the high-dynamic range Femto photoreceiver.

2.1.1 Microscope design

An IR microscope is installed to provide a top-view of the PIC for alignment and diagnostic visualization. The microscope consists of a Mitutoyo MY10X-823 objective lens, a $f=100$ μm tube lens, and a Goldeye G-130 VSWIR camera with 656×520 pixel resolution at 5 μm pixel pitch. This provides a magnification of $5\times$, which translates to an on-chip resolution limit of 1 μm . A pen-type visible-light borescope from Vividia is installed to provide a side-view of the optical fiber alignment to the PIC. Figure 3 shows a photo of the NIR microscope, a photo of the input gratings taken with the top-view IR microscope, and a photo of optical fibers aligned to the PIC taken with the side-view borescope.

2.1.2 Telescope pupil to PIC injection

A key feature of the Ames photonics testbed is the ability to couple light from a realistic telescope pupil onto the PIC to demonstrate the AstroPIC coronagraph robustness to input pupil shape and wavefront errors. To meet this requirement, a pupil reimaging and compression system has been designed in ZEMAXTM to compress a 3 mm diameter aperture telescope pupil by a factor of 10 to 300 μm . The reimaged and compressed pupil is sampled by a 3×3 rectangular grid microlens array, which has a 100 μm pitch to match the grating couplers spacing shown in Figure 4. We selected the VIAVI MLA-S100-f4 off-the-shelf microlens array operating at $f/4.2$ which is close to the $f/5$ lens needed to match the size of the grating coupler mode. The lenses are illuminated at a 12 degree angle (in air) to match the grating coupler design angle of incidence (10 degrees in the SiO_2 cladding). The flat side of the lenses is the first optical surface and the curved surface of the lenses points down towards the grating couplers. This part of the setup is still in progress and will be implemented in the Fall of 2025.

2.1.3 Testbed control software

A suite of instrument drivers and a custom GUI application are being developed in Python to control and readout data from the laser, TEC controller, and NI DAQ during experiments. Figure 5 shows a screenshot of the GUI application during an experiment, which displays plots of the monitor and data photodetector readouts and telemetry from the laser and TEC controller. Each phase shifter has a corresponding control widget that has options to set an input voltage, sweep the full voltage range, calibrate the phase shifter, and minimize a

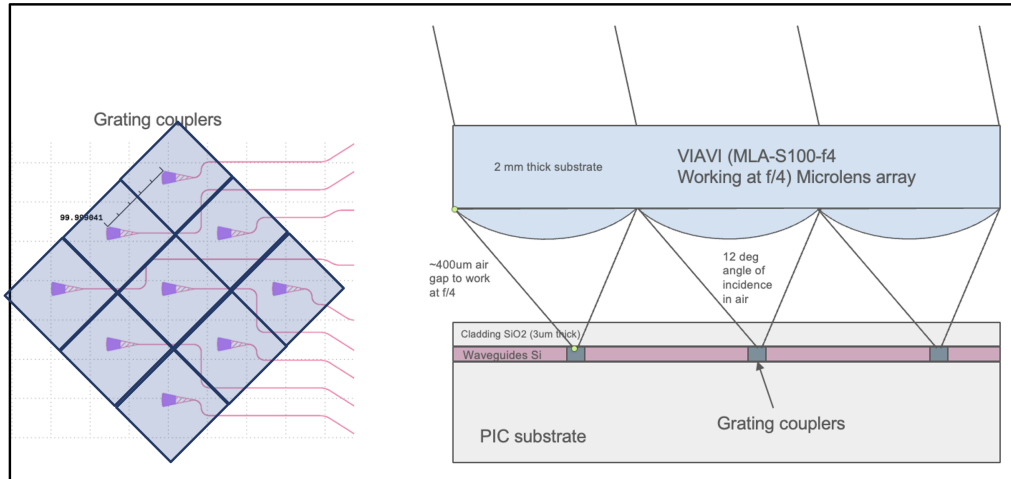


Figure 4. Schematic of the pupil injection in grating couplers using microlenses.

single output channel. The GUI also includes a visualization of the MZI mesh that displays the channel number corresponding to each phase shifter location.

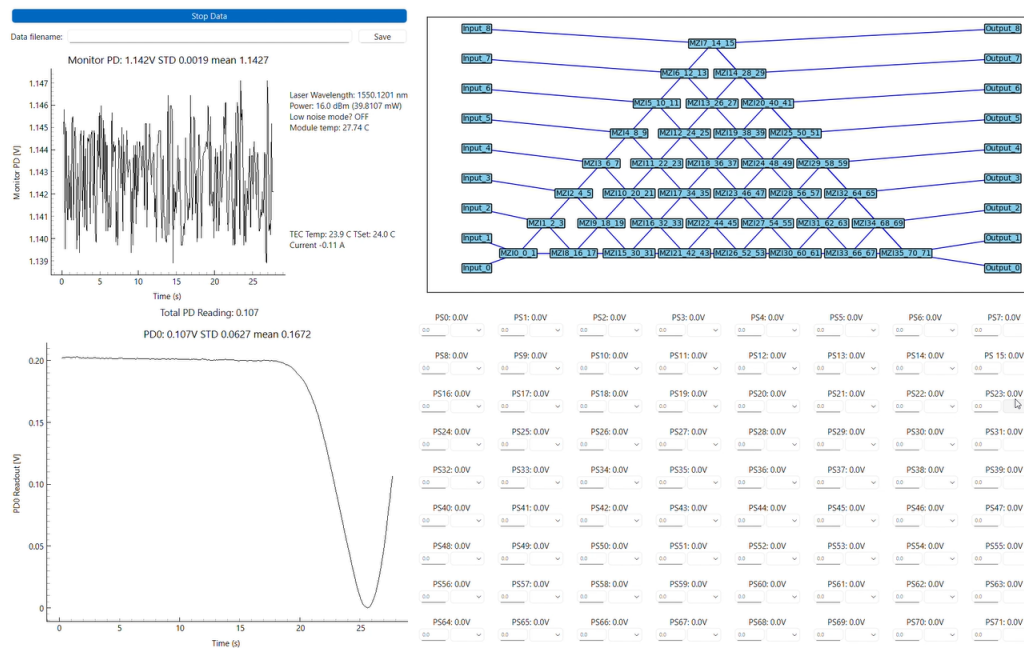


Figure 5. Screenshot of the lab GUI during a measurement of a voltage sweep on phase shifter 15 with the input fiber aligned to input 8 and the output fiber aligned to output 0. The GUI displays (counterclockwise from top left): the monitor tap port photodetector readout, telemetry from the TEC and the laser controllers, the data photodetector readout, individual control buttons for each phase shifter, and a visualization to map each phase shifter number to its location in the mesh.

2.2 PIC Design and Fabrication

The first AstroPIC design iteration includes two coronagraph mesh designs, a 9-channel full triangular photonic mesh and a 7-channel 4-diagonal mesh with multi-stage MZIs, as well as various photonic component test structures. This design layout (shown in Figure 6) was fabricated with two different foundries, the Advanced Micro Fabrication (AMF) foundry in Singapore and Applied Nanotools (ANT) in Canada. The layouts for

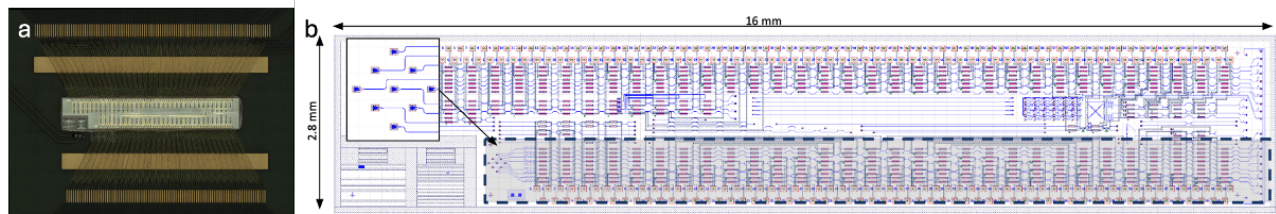


Figure 6. (a) Photo of AstroPIC coronagraph prototype chip wirebonded to the host PCB. (b) Screenshot of the PIC layout showing the 9-channel full triangular mesh with a zoom-in on the 3×3 input grating array inset.

both foundry runs were nearly identical, with the same set of meshes and test structures fabricated using each foundry's standard silicon photonics process flow with 220 nm tall \times 500 nm wide silicon slab waveguides in silicon dioxide cladding, thermal phase shifters, and air trenches between heaters. There are differences in the design rules and fabrication approach of both foundries, the most notable of which is that AMF uses photolithography while ANT uses electron beam lithography to pattern waveguide features. Photolithography tends to be more cost-effective and scalable, while electron beam lithography is more flexible and can accommodate smaller feature sizes and more flexible layer heights, which enabled the high-efficiency grating design described in Valdez et al. 2025.¹² Preliminary experiments do not show significant differences in throughput or coronagraph performance between devices fabricated with both foundries, differences in single-channel minimization experiment results are attributed to the thermal phase shifter resistance being higher for ANT chips compared to AMF chips.

2.3 Optical Power Budget

Table 2 summarizes the optical power budget for the testbed. The AstroPIC chip is measured to have a total optical power throughput of -10.2 dB (9.5%) for an AMF chip and -10.6 dB (8.7%) for an ANT chip using cleaved optical fibers for input/output coupling to the grating couplers. The full testbed has a measured total throughput of -11.2 dB (7.6%) with the AMF chip, which means that the testbed has a measurable dynamic range of ~ 105 dB (3.2×10^{-11} contrast ratio) with an input laser power of 16 dBm, which is sufficient to measure the target contrast ratio for measuring Earth-like planets around Sun-like stars (100 dB extinction, or 1×10^{-10} contrast ratio). This throughput was measured with chip samples from both AMF and ANT with similar results, as shown in Table 2. We expect the coupling loss from a free-space pupil input through the lenslet array to be ~ 1.5 dB less efficient than the current single fiber input used in the setup based on the simulations described in Section 3.1. This would lead to an predicted instrument throughput of -11.7 dB (6.7%) and a 100 dB-minimized channel optical power of -96.7 dBm, which is still above the minimum detectable power for the setup.

Table 2. Optical power budget for the AstroPIC testbed with the current prototype PIC design. Measurements of grating coupler and on-chip losses are included for chip samples fabricated by both AMF and ANT foundries. The predictions of maximum and minimum power in the output channel correspond to the AMF measurements.

Parameter	Value
Input laser power	16 dBm (40 mW)
Fiber/free-space optics losses	1 dB
Grating coupler losses (per coupler)	4.1 dB (AMF), 4.5 dB (ANT)
On-chip losses	2 dB (AMF), 1.6 dB (ANT)
Max. power in output channel	4.8 dBm (3 mW)
Min. power in output channel (100 dB extinction)	-95.2 dBm (300 fW)
Minimum detectable power, signal channel	-100 dBm (100 fW)

3. TESTBED SIMULATION DEVELOPMENT

In addition to the experimental control software, a “hardware simulator” is being developed to emulate the behavior of the testbed to provide a theoretical model to compare the experimental results to and to test more advanced algorithms for mesh control.⁹ The hardware simulator models the full end-to-end system including

coupling from an optical fiber or telescope pupil into the chip, the performance of the on-chip mesh with applied voltages on the phase shifters, and the readout of each output channel photodiode.

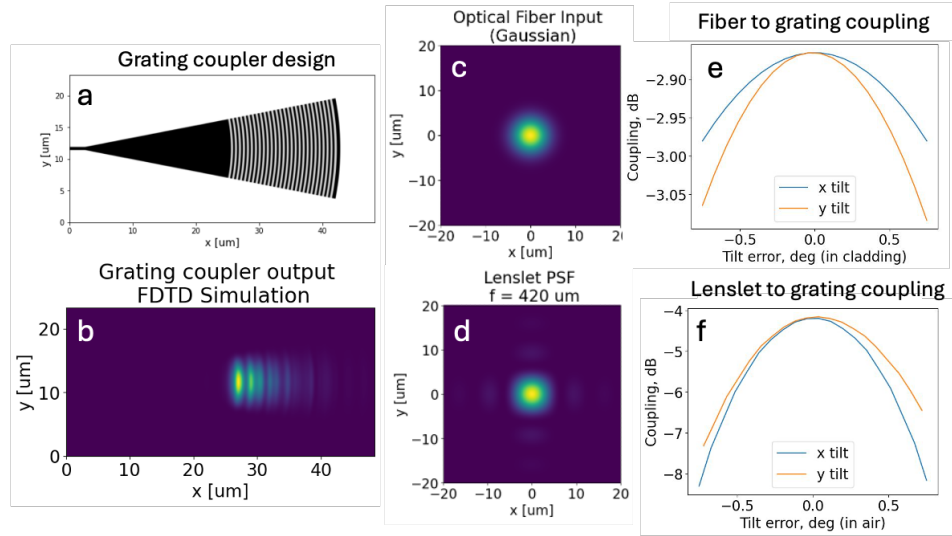


Figure 7. (a) Grating coupler design and (b) top-view FDTD simulation of the grating coupler output electric field. Simulated electric field profiles for a (c) single fiber Gaussian input and (d) the lenslet PSF. Overlap power coupling results as a function of tilt error in x and y for the grating coupler output field with (e) single fiber Gaussian field and (f) lenslet PSF field.

3.1 Input Coupling Model

The electric field coupling efficiency η_E is modeled by computing the scalar overlap integral between the incident optical field E_1 and the optical field output of the grating coupler E_2 :

$$\eta_E = \frac{\int E_1 \times E_2^* \cdot dS}{\sqrt{\int E_1 \times E_1^* \cdot dS \int E_2 \times E_2^* \cdot dS}}$$

The incident field is assumed to be linearly polarized transverse to the waveguide direction (along the y-axis in Figure 7a) in order to couple into the quasi-TE mode of the waveguide. For a single fiber input, the incident field is modeled as a Gaussian beam with a beamwaist radius of 5.2 μm , corresponding to a Thorlabs SMF-28 single-mode fiber at 1550 nm wavelength,^{*} shown in Figure 7c. For free-space input with the microlens array, a diffraction model was developed with the HCIPy package¹³ to calculate the point-spread function of a single lenslet. The incident pupil is modeled in HCIPy and sub-sampled assuming a rectangular array of lenslets with 100 μm pitch. The lenslet shape is assumed to be a spherical lens with a focal length of 420 μm . A geometric optics model is performed in ZEMAXTM to calculate the predicted geometric aberrations that result from propagating through the lenslet at an incidence angle of $\sim 12^\circ$; these aberrations are applied as a phase screen in the diffraction model. Another phase screen is applied to account for the effect of incident field tilt. Figure 7d shows the predicted PSF for a single lenslet including the effect of these aberrations.

The grating coupler output field is found through a finite-difference time-domain (FDTD) model using the open-source Python electromagnetic solver Emopt,¹⁴ shown in Figure 7b. The results of the overlap calculation for a single fiber or free-space input with this grating coupler field are shown in Figure 7e-f. The optical power coupling efficiency is found by squaring the electric field coupling result. This model predicts an input coupling loss of ~ 3 dB (50% coupling efficiency) for a single fiber input and ~ 4 dB (40% coupling efficiency) with perfect alignment, and slightly higher losses as incident tilt error is increased. The free-space coupling with the lenslet

^{*}Specifications for SMF28 fiber at 1550 nm can be found on the Thorlabs website: https://www.thorlabs.com/newgrouppage9.cfm?objectgroup_id=334

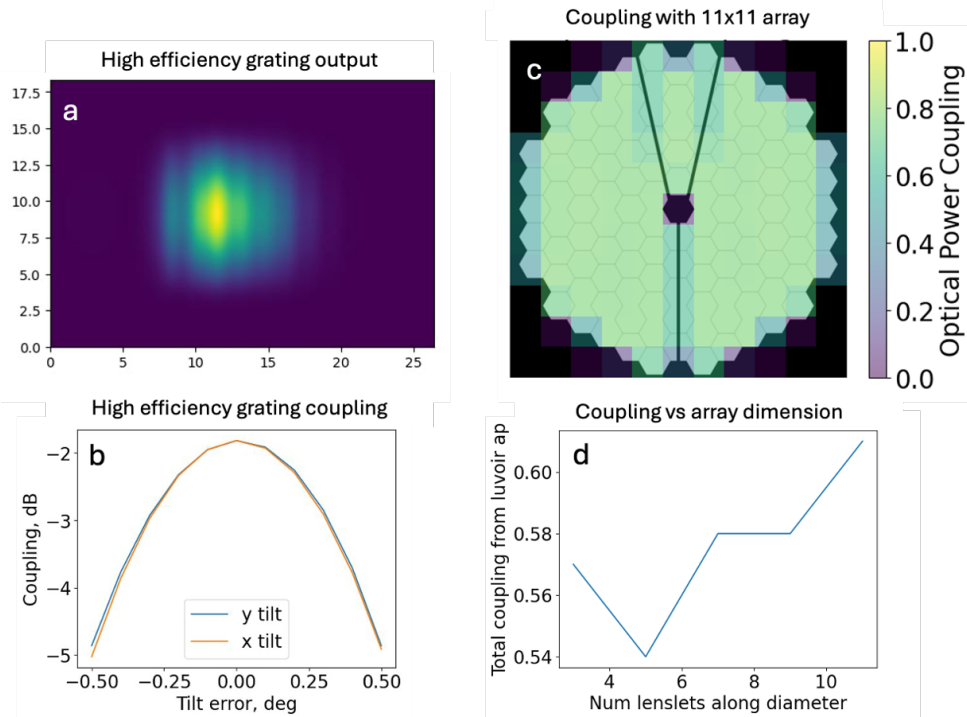


Figure 8. (a) Top-view FDTD simulation result for the high efficiency grating coupler design¹⁵ and (b) predicted power coupling from the free-space lenslet PSF input as a function of tilt error in x and y. (c) Plot of optical power coupling from a LUVOIR-like aperture for each lenslet/grating coupler in an 11x11 array overlaid with the aperture pupil shape. (d) Total power coupling as a function of lenslet array dimension.

is more sensitive to tilt errors compared to the Gaussian fiber input. This model does not account for the effects of reflections at the cladding-air interface, fabrication imperfections in the grating or waveguide, or imperfect alignment or cleaving of the optical fiber, which can account for the ~ 1 dB difference between these simulation predictions and the 4.1 dB coupling loss measured in lab with a cleaved optical fiber for input/output.

This input coupling model is useful for predicting the impact of different pupil geometries and microlens array dimensions on the total throughput and behavior of the device. We have repeated the coupling calculation for a more advanced grating coupler design that uses multiple etch layers to increase the efficiency and enable coupling of light from a normal incidence into the waveguide.¹⁵ This grating design was recently demonstrated in the lab to provide 85.4% (-0.69 dB) coupling efficiency over a 20 nm 1-dB bandwidth around a central wavelength of 1546 nm,¹² which would increase the end-to-end throughput of the 9-channel AstroPIC instrument from the current value of $\sim 10\%$ to $\sim 50\%$. Figure 8c-d shows the predicted coupling efficiency for this improved grating design with an obstructed LUVOIR-like telescope aperture using input microlens/coupler arrays of different dimensions. These simulations show that lenslets that sample obstructed pupil regions have lower coupling efficiency, and that increasing the sampling resolution through having more microlens/grating coupler channels can improve the total coupling efficiency by a few percent. Figure 8b shows that coupling into this grating design is slightly less sensitive to tip/tilt error than the current grating design shown in Figure 7f. Similar analysis using the current grating coupler design predicts an input coupling efficiency of $\sim 30\%$ for this LUVOIR-like telescope aperture sampled with the 3x3 microlens and grating coupler array used in lab.

3.2 Mesh Simulation

Once the input field coupling is predicted, a full mesh simulator is used to propagate the input through the device and predict the readout on each output channel photodetector. The mesh transfer function calculation is described in detail in Fogarty et al. 2025⁹ and the normalized intensity ($|E|^2$) in each channel is calculated, which gives the fraction of the total input optical power that reaches each output. This is converted to the photodetector

readout using the responsivity and gain formulas provided by the vendors. This mesh model is integrated into the hardware simulator to enable the lab GUI application to run realistic simulations of testbed experiments. In the future, this model will be expanded to include more accurate noise terms on the photodetectors and models of other sources of error such as thermal crosstalk and stray light. The goal is to eventually enable model-based control of the AstroPIC device to achieve better performance with less configuration time.

4. EXPERIMENTAL RESULTS

The Ames photonics testbed achieved first light with a PIC coronagraph in July 2025 using the chip shown in Figure 6a. Figure 6b shows the layout of the first AstroPIC chip design, which contains two variations of a PIC coronagraph mesh as well as several test structures to test individual components. The testbed is first being used to characterize the 9-channel full triangular mesh with a 3x3 square array of input grating couplers and a line of 9 output grating couplers.

4.1 Testbed Characterization

Initial testing of the AstroPIC coronagraphs use a single optical fiber at the input and output; the full free-space coupling with a telescope pupil and microlens array is expected to be implemented in the early Fall of 2025. The goal of the tests presented here is to characterize the performance of the components and systems on the chip and in the testbed and identify promising areas of improvement for future iterations of the chip and testbed designs.

The input/output coupling losses were measured by aligning the input and output optical fibers to a grating loss test structure that consists of an input grating coupler, a straight waveguide with a length of 2.8 mm, and an output grating coupler. This measurement was compared to a measurement of the input fiber aligned directly to the output fiber and divided by two to give the coupling loss per grating of 4.1 dB on an AMF chip and 4.5 dB on an ANT chip (note: this calculation assumes the input/output grating couplers have equal loss, which is a reasonable approximation for grating couplers on the same chip sample). The total on-chip loss was calculated by comparing the maximum signal measured through the full mesh to the grating loss test structure measurement. The difference in these two measurements was 2 dB for the AMF chip and 1.6 dB for the ANT chip, which agrees with the expected waveguide propagation loss of $\sim 1 - 2$ dB/cm for both chips.

A single MZI test structure is used to characterize the performance of the key photonic building block in response to a voltage sweep. The results of this calibration are shown in Figure 9 for an AMF chip, with measured extinction ratios of 28 dB in the bar configuration (output port is in line with input port) and 44 dB in the cross configuration (output port is across from input port). Using a phase shifter resistance value of 750 Ohms, we find that a 2π phase shift is achieved with an applied voltage of ~ 8 V, corresponding to ~ 85 mW of power draw.

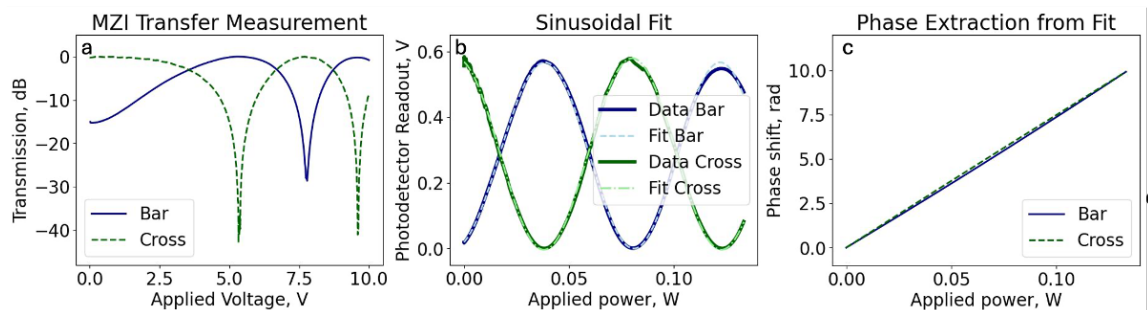


Figure 9. (a) Measurement of MZI response to an applied voltage sweep in bar (top right input, top left output) and cross (top right input, bottom left output) configuration. (b) Sinusoidal fit to MZI transfer data and (c) extracted phase shift vs applied power for data from both bar and cross output ports.

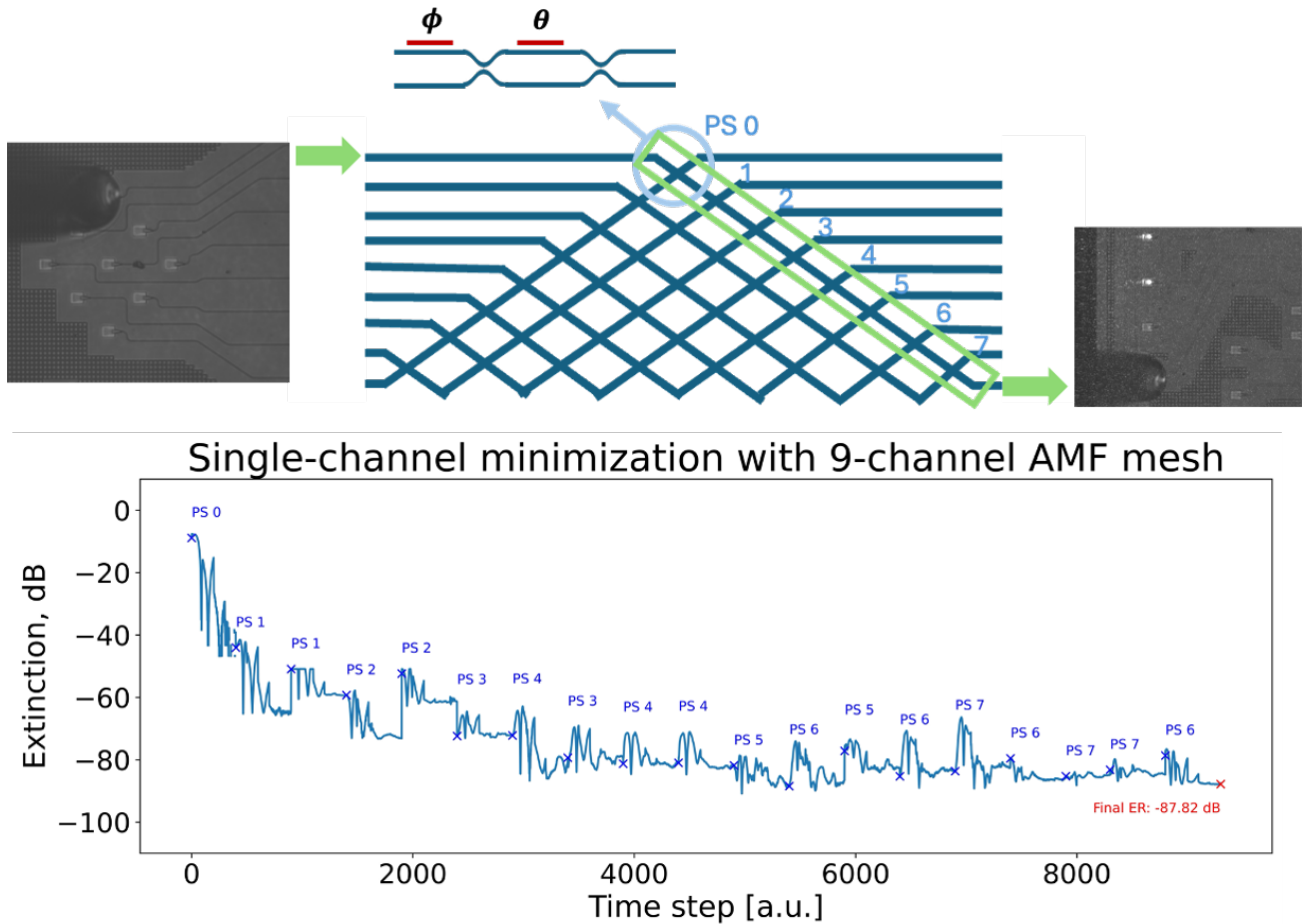


Figure 10. (Top) Visualization of single-channel minimization experiment: (from left) Microscope image of input fiber alignment, diagram of 9-channel full triangular mesh with the top diagonal and corresponding theta phase shifter labels indicated and a diagram of single MZI element inset, and microscope image of output fiber alignment. (Bottom) Data from single-channel minimization experiment using a chip fabricated by AMF over 19 minimization iterations along the top diagonal achieving a final extinction ratio (ER) of > 87 dB (contrast ratio $< 2 \times 10^{-9}$). The time is listed in timesteps (arbitrary units); each time step is approximately 0.12 s and the full experiment took around 45 minutes, including time to periodically realign the input and output fibers between the 1-minute long minimization routines for each phase shifter. The ‘PS #’ labels indicate the theta phase shifter being controlled during each iteration, and the discontinuities between iterations are due to periodic realignment of the input and output fibers.

4.2 Single Channel Minimization

The first type of coronagraph experiment performed with the Ames testbed used a single fiber at the input and output to demonstrate minimizing a single illuminated input channel to achieve the highest extinction possible in a single output channel. For actual coronagraphic functionality, light from as many input channels as possible would be minimized by sorting starlight into as few output channels as possible. The single-channel minimization experiments presented in this paper are an important intermediate step towards this goal.

Figure 10 shows the setup and results of this experiment, where the top input grating was illuminated and the bottom output grating was measured so that a single diagonal with 8 MZIs could be tuned to minimize the signal reaching the output channel. Since we use a single illuminated input, we only need to control the θ phase shifter of each MZI to minimize the output channel. The minimization routine followed the procedures described in Valdez et al. 2025,¹⁶ where the optimal voltage for each phase shifter was found iteratively by sweeping the voltage across progressively smaller voltage ranges around the minimum state until the voltage sweep step size

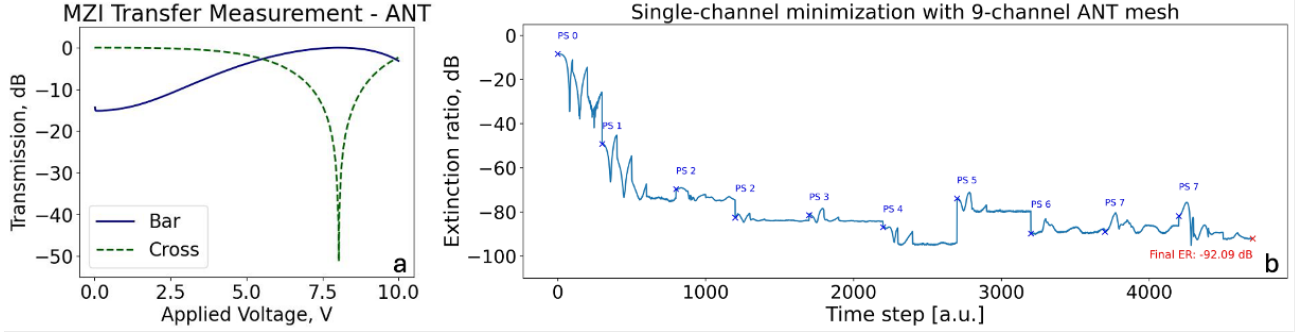


Figure 11. (a) MZI transfer measurement using a chip fabricated by ANT showing an extinction ratio of > 50 dB for a single MZI. (b) Data from single-channel minimization experiment using the same chip fabricated by ANT reaching a final extinction ratio of 92 dB (contrast ratio 6×10^{-10}). This experiment took approximately 15 minutes, including time to realign the input and output fibers between 1-minute long minimization routines for each phase shifter. The 'PS #' labels indicate the theta phase shifter being controlled during each iteration, corresponding to the labels in Figure 10 (top).

reached the resolution limit of the DAQ (0.3 mV). This procedure takes about a minute to complete for each MZI. The total extinction ratio is calculated by dividing the signal measured in the output channel by the sum of the signals measured across all channels. The baseline total signal measurement across all channels was repeated before and after the minimization procedure, and the difference between these measurements was below 0.2 dB ($< 5\%$). The input and output fibers were observed to drift over the course of the experiment, so this alignment was re-optimized periodically by setting the top MZI to a "cross" state to direct a higher signal to the output channel and maximizing the coupling with the high signal before re-minimizing the top channel and continuing with the experiment.

The AstroPIC instrument was extremely efficient at minimizing a single channel input, demonstrating an extinction ratio of over 87 dB (contrast ratio $< 2 \times 10^{-9}$) using a chip fabricated by AMF. Figure 10 shows the measured extinction ratio in the output channel over the course of the experiment. It can be seen that the majority of the suppression comes from minimizing the first 4 MZIs in the diagonal, and that the high suppression remained stable across many time steps during each experiment. The jumps in extinction ratio between phase shifter minimization iterations occur due to realigning the input and output fibers. The uncertainty in this measurement is 0.5 dB (10%), which is calculated from the standard deviation of the signal measurement over 30 seconds at the end of the minimization procedure (6%) and the difference in the total on-chip optical power measurement repeated before and after the minimization routine (5%).

Figure 11 shows the same experiment repeated using a chip fabricated by ANT. In this case, the thermal phase shifters had a slightly higher resistance compared to the AMF phase shifters, which lead to a larger voltage required to achieve the "cross" state. This meant that the MZI was not able to reach a full 2π sweep in phase, but also spread the DAQ control resolution over a smaller phase range compared to the AMF experiment, meaning that a deeper extinction ratio of > 50 dB could be reached for a single MZI (see Figure 11(a)). This improved resolution and MZI performance led to a higher final extinction ratio of 92 dB (contrast ratio 6×10^{-10}) using fewer iterations compared to experiments with the AMF chip, shown in Figure 11(b). The uncertainty of this measurement is 0.4 dB (10%) based on the standard deviation of the post-minimization signal measurement over 30 seconds (4%) and the difference between initial and final total power measurements (6%). The experiment is currently limited by alignment stability and stray light in the chip, which makes measuring such a small signal with confidence challenging. The characteristic transfer function of the MZI in response to an applied voltage sweep provides a convenient way to validate that the measured extinction of the signal is coming from the desired waveguide channel and not stray light due to misalignment of the input/output fibers.

5. CONCLUSION

Initial laboratory testing has validated the AstroPIC concept by demonstrating 92 ± 0.4 dB extinction of a single input channel at 1550 μm wavelength. High extinction ratios were measured using PIC chip samples fabricated

by two different foundries, demonstrating the repeatability and flexibility of the instrument technology. These promising initial results demonstrate the potential of the AstroPIC coronagraph concept for enabling high-contrast measurements of exoplanets. Achieving a contrast ratio on the order of 6×10^{-10} with bulk optics technology requires precise optical systems with advanced thermal control, typically operated in vacuum.^{5,17} These demonstrations of extremely high mode suppression in a standard laboratory environment show the power of integrated photonics technology to manipulate light with high precision using systems that are significantly smaller and less complex than traditional bulk optics designs.

Experiments with the AstroPIC coronagraph testbed at NASA Ames Research Center are ongoing. The next steps for the project are to assemble the pupil injection optics, bond the output fiber array, and install the microlens array to enable coronagraph experiments with realistic HWO-like pupils. The testbed will then be used to test control algorithms targeting high contrast across a broader optical bandwidth.⁹ In the future, the AstroPIC project will be extended to have more channels to enable a larger field of view for the instrument and higher throughput by incorporating a higher-efficiency grating coupler design.¹² Another key challenge is improving the optical bandwidth performance through a combination of broader band component design, additional degrees of freedom in the mesh design, and tiling of multiple chips. The team is also working to combine experimental results with instrument simulations to inform the next generation AstroPIC prototype design.

ACKNOWLEDGMENTS

This work was carried out at NASA Ames Research Center and Stanford University's ECE department. The AstroPIC project is supported through NASA STMD's Early Career Initiative (ECI) program.

REFERENCES

- [1] Minardi, S., Harris, R. J., and Labadie, L., "Astrophotonics: astronomy and modern optics," *Astronomy and Astrophysics Review* **29**(6) (2021).
- [2] Reck, M., Zeilinger, A., Bernstein, H. J., and Bertani, P., "Experimental realization of any discrete unitary operator," *Physical Review Letters* **73**(1), 58–61 (1994).
- [3] Miller, D. A. B., "Self-configuring universal linear optical component [invited]," *Photonics Research* **1**(1), 1–15 (2013).
- [4] Guyon, O., Pluzhnik, E. A., Kuchner, M. J., Collins, B., and Ridgway, S. T., "Theoretical limits on extrasolar terrestrial planet detection with coronagraphs," *The Astrophysical Journal Supplement Series* **167**(1) (2006).
- [5] Belikov, R., Sirbu, D., Jewell, J. B., Guyon, O., and Stark, C. C., "Theoretical Performance Limits for Coronagraphs on Obstructed and Unobstructed Apertures: How Much Can Current Designs be Improved?," in [*Techniques and Instrumentation for Detection of Exoplanets X*], Shaklan, S. B. and Ruane, G. J., eds., **11823**, 118230W–1, International Society for Optics and Photonics, SPIE (2021).
- [6] Jewell, J. B., Wallace, J. K., Costa, L., McKeithen, D. M., Wenger, T. S., and Briggs, R. M., "A photonic coronagraph architecture achieving theoretical near ideal performance," in [*Space Telescopes and Instrumentation 2024: Optical, Infrared, and Millimeter Wave*], **13092**, 130921S, International Society for Optics and Photonics, SPIE (2024).
- [7] McKeithen, D., Jewell, J., and Wallace, J. K., "Hardware development towards the demonstration of an ideal photonic coronagraph," in [*Space Telescopes and Instrumentation 2024: Optical, Infrared, and Millimeter Wave*], **13092**, 130925V, International Society for Optics and Photonics, SPIE (2024).
- [8] Fineberk, L., Zeimer, J., Ansdell, M., Crooke, J., Dressing, C., Mennesson, B., O'Meara, J., Pepper, J., and Roberge, A., "The Habitable Worlds Observatory engineering view: status, plans, and opportunities," in [*Space Telescopes and Instrumentation 2024: Optical, Infrared, and Millimeter Wave*], **13092**, 130921N, SPIE (2024).
- [9] Fogarty, K., Sirbu, D., Morgan, R., Bendek, E., and Belikov, R., "Modelling and Optimization Pipeline for the AstroPIC Coronagraph," in [*SPIE Optics and Photonics*], **13627**, 13627–82, SPIE (2025).

- [10] Sirbu, D., Belikov, R., Valdez, C., Sun, Z., Kroo, A., Solgaard, O., Miller, D. A. B., and Guyon, O., “AstroPIC: Near-Infrared photonic integrated circuit coronagraph architecture for the Habitable Worlds Observatory,” in [*Space Telescopes and Instrumentation 2024: Optical, Infrared, and Millimeter Wave*], **13092**, 130921T, SPIE (2024).
- [11] Sirbu, D., Belikov, R., Bendek, E., Fogarty, K., Morgan, R., Sims, K., Valdez, C., Kroo, A., Vlk, M., Solgaard, O., and Miller, D. A. B., “AstroPIC II: overview of technology development for a near-infrared photonic integrated coronagraph for the Habitable Worlds Observatory,” in [*SPIE Optics and Photonics*], **13623**, 13623–15, SPIE (2025).
- [12] Valdez, C. G., Bongarz, S. A., Kroo, A. R., Miller, A. J., Digonnet, M. J. F., Miller, D. A. B., and Solgaard, O., “Three-wave interaction grating coupler with sub-decibel insertion loss at normal incidence,” (2025).
- [13] Por, E. H., Haffert, S. Y., Radhakrishnan, V. M., Doelman, D. S., van Kooten, M., and Bos, S. P., “High Contrast Imaging for Python (HCIPy): an open-source adaptive optics and coronagraph simulator,” in [*Adaptive Optics Systems VI*], **10703**, 1070342, SPIE (2018).
- [14] Michaels, A., “Emopt: Electromagnetic optimization toolbox.” <https://github.com/anstmichaels/emopt> (2018).
- [15] Valdez, C. G., Pai, S., Broaddus, P., and Solgaard, O., “High-efficiency vertically emitting coupler facilitated by three wave interaction gratings,” *Optics Letters* **49**, 2373–2376 (2025).
- [16] Valdez, C. G., Sun, Z., Kroo, A. R., Miller, D. A. B., and Solgaard, O., “High-contrast nulling in photonic meshes through architectural redundancy,” *Optics Letters* **50**, 3660–3663 (2025).
- [17] Mennesson, B., Belikov, R., Por, E., and et al., “Current laboratory performance of starlight suppression systems and potential pathways to desired habitable worlds observatory exoplanet science capabilities,” *J. Astron. Telesc. Instrum. Syst.* **10**(3), 035004 (2024).